

## Ferroelectricity in $\text{Pb}_{1+\delta}\text{ZrO}_3$ Thin Films

Ran Gao,<sup>†</sup> Sebastian E. Reyes-Lillo,<sup>‡,§</sup> Ruijuan Xu,<sup>†</sup> Arvind Dasgupta,<sup>†</sup> Yongqi Dong,<sup>¶,⊥</sup> Liv R. Dedon,<sup>†</sup> Jieun Kim,<sup>†</sup> Sahar Saremi,<sup>†</sup> Zuhuang Chen,<sup>†,■</sup> Claudy R. Serrao,<sup>||</sup> Hua Zhou,<sup>¶</sup> Jeffrey B. Neaton,<sup>‡,§,□</sup> and Lane W. Martin<sup>\*,†,■</sup>

<sup>†</sup>Department of Materials Science and Engineering, <sup>§</sup>Department of Physics, and <sup>||</sup>Department of Electrical Engineering and Computer Sciences, University of California, Berkeley, California 94720, United States

<sup>‡</sup>Molecular Foundry, and <sup>■</sup>Materials Sciences Division, Lawrence Berkeley National Laboratory, Berkeley, California 94720, United States

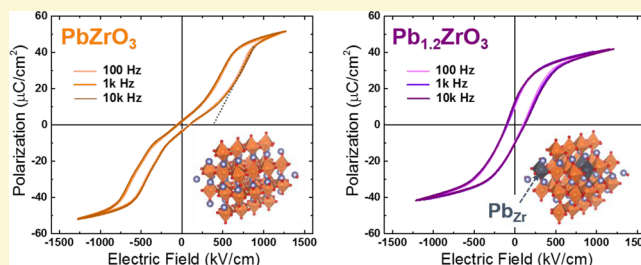
<sup>¶</sup>X-ray Science Division, Advanced Photon Source, Argonne National Laboratory, Argonne, Illinois 60439, United States

<sup>⊥</sup>National Synchrotron Radiation Laboratory and CAS Key Laboratory of Materials for Energy Conversion, University of Science and Technology of China, Hefei, Anhui 230026, P. R. China

<sup>□</sup>Kavli Energy NanoSciences Institute at Berkeley, Berkeley, California 94720, United States

### Supporting Information

**ABSTRACT:** Antiferroelectric  $\text{PbZrO}_3$  is being considered for a wide range of applications where the competition between centrosymmetric and noncentrosymmetric phases is important to the response. Here, we focus on the epitaxial growth of  $\text{PbZrO}_3$  thin films and understanding the chemistry–structure coupling in  $\text{Pb}_{1+\delta}\text{ZrO}_3$  ( $\delta = 0, 0.1, 0.2$ ). High-quality, single-phase  $\text{Pb}_{1+\delta}\text{ZrO}_3$  films are synthesized via pulsed-laser deposition. Although no significant lattice parameter change is observed in X-ray studies, electrical characterization reveals that while the  $\text{PbZrO}_3$  and  $\text{Pb}_{1.1}\text{ZrO}_3$  heterostructures remain intrinsically antiferroelectric, the  $\text{Pb}_{1.2}\text{ZrO}_3$  heterostructures exhibit a hysteresis loop indicative of ferroelectric response. Further X-ray scattering studies reveal strong quarter-order diffraction peaks in  $\text{PbZrO}_3$  and  $\text{Pb}_{1.1}\text{ZrO}_3$  heterostructures indicative of antiferroelectricity, while no such peaks are observed for  $\text{Pb}_{1.2}\text{ZrO}_3$  heterostructures. Density functional theory calculations suggest the large cation nonstoichiometry is accommodated by incorporation of antisite  $\text{Pb}_{\text{Zr}}$  defects, which drive the  $\text{Pb}_{1.2}\text{ZrO}_3$  heterostructures to a ferroelectric phase with  $R3c$  symmetry. In the end, stabilization of metastable phases in materials via chemical nonstoichiometry and defect engineering enables a novel route to manipulate the energy of the ground state of materials and the corresponding material properties.



## INTRODUCTION

The antiferroelectric perovskite  $\text{PbZrO}_3$  is regarded as a promising candidate for applications in energy storage,<sup>1</sup> electrothermal energy conversion,<sup>2,3</sup> and transducers.<sup>4,5</sup> In the bulk,  $\text{PbZrO}_3$  is able to undergo an electric-field-induced, first-order phase transition from a nonpolar ground state to a metastable polar state, as manifested by a double-hysteresis loop.<sup>6,7</sup> This antiferroelectric behavior arises from structural distortions and complex lattice dynamics, namely cooperative antiparallel displacements of the lead ions and antiferrodistortive octahedral rotations, and is manifested as nearly energy-degenerate centrosymmetric, antiferroelectric and noncentrosymmetric, ferroelectric states.<sup>8–12</sup> Because of the small free energy difference between the phases, the system is highly susceptible to perturbations including electric fields, point defects,<sup>13,14</sup> lattice distortions,<sup>15,16</sup> and electrostatic boundary conditions,<sup>17–19</sup> which can tip the balance of the ground state energy competition.

Thus, it is important to understand the effect of these perturbations to better control and engineer  $\text{PbZrO}_3$  for future applications and to synthesize the material in a controllable way such that the desired properties are achieved. In the past decades, although various routes, such as chemical substitution,<sup>20</sup> epitaxial strain,<sup>21–24</sup> and size effects,<sup>19,25</sup> have been studied to modify and control the ground state of  $\text{PbZrO}_3$ , the impact of cation nonstoichiometry has rarely been explored. There is growing evidence that cation nonstoichiometry can play a significant role in the evolution of material properties as has been highlighted in, for example,  $\text{SrTiO}_3$ ,<sup>26–28</sup>  $\text{BaTiO}_3$ ,<sup>29,30</sup> and  $\text{BiFeO}_3$ .<sup>31</sup> This is particularly important in perovskite systems where the polarization and lattice modes are strongly coupled, and, thus, local nonstoichiometry and lattice imperfection can distort the structure and drive the material

Received: June 16, 2017

Revised: July 14, 2017

Published: July 16, 2017

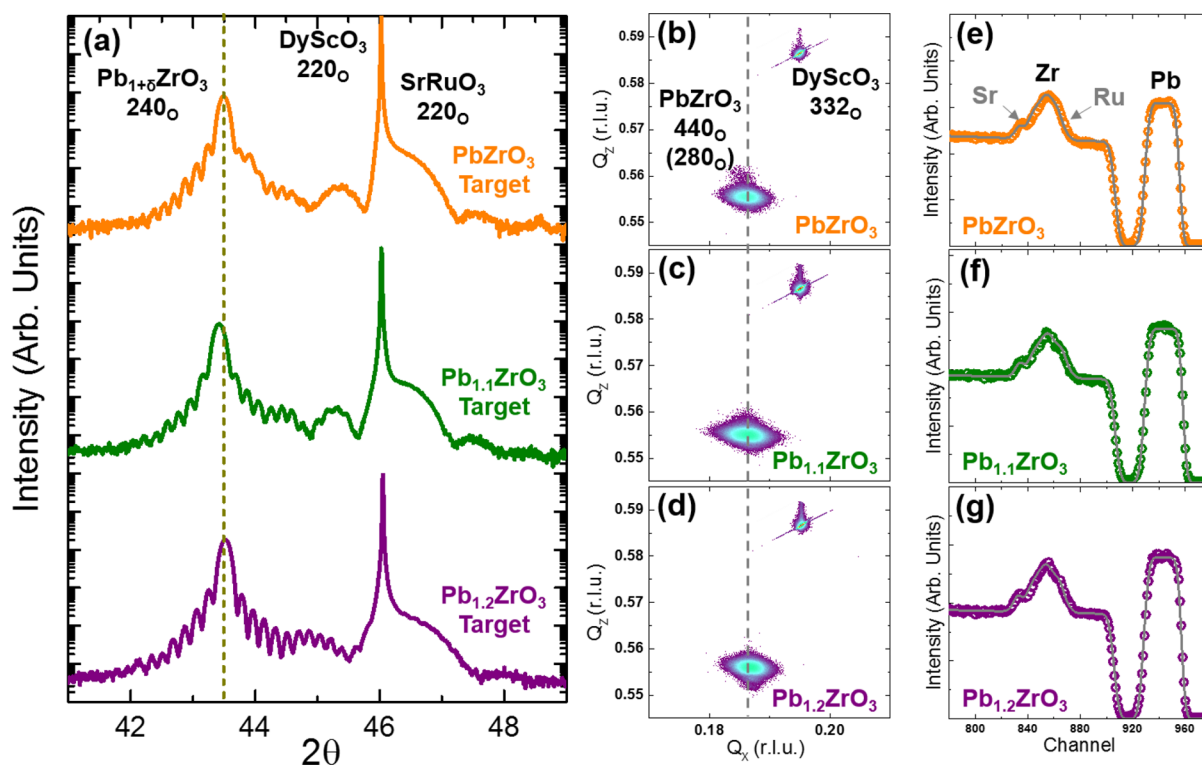


**Figure 1.** (a) X-ray  $\theta$ - $2\theta$  line scans reveal high-quality  $(120)_O$ -oriented, 50 nm thick  $Pb_{1+\delta}ZrO_3$  ( $\delta = 0, 0.1, \text{ and } 0.2$ ) films on 10 nm  $SrRuO_3$ / $DyScO_3$   $(110)$  substrates. Reciprocal space mapping studies about the  $332_O$ - and  $440_O$  ( $280_O$ )-diffraction conditions of the substrate and film, respectively, for the (b)  $PbZrO_3$ , (c)  $Pb_{1.1}ZrO_3$ , and (d)  $Pb_{1.2}ZrO_3$  heterostructures reveal nearly completely relaxed epitaxial  $Pb_{1+\delta}ZrO_3$  films with similar lattice parameters. Rutherford backscattering spectrometry studies reveal film chemistries of (e)  $PbZrO_3$ , (f)  $Pb_{1.1}ZrO_3$ , and (g)  $Pb_{1.2}ZrO_3$ , for growth from targets of the same chemistries.

into exotic ground states. For instance, in nonstoichiometric  $Sr_{1-\delta}TiO_3$  thin films, local Sr-deficiency is thought to perturb the lattice and give rise to relaxor-like behavior.<sup>28,32</sup> It has also been reported that in ferroelectric  $BaTiO_3$  thin films, local lattice imperfection and aligned defect dipoles can induce dramatic changes in the ferroelectric-to-paraelectric phase transition temperature.<sup>33</sup> Thus, the effect of cation nonstoichiometry, where local cation excess or deficiency and lattice distortions are expected, could have a significant impact on antiferroelectric  $PbZrO_3$  where multiple lattice instabilities are involved in determining the final ground state. Additionally, in  $PbZrO_3$ , previous work has already found that the system is prone to antisite defects (i.e., lead ions replacing zirconium ions).<sup>34–37</sup> This tendency for antisite defects, and the fact that to acquire high-quality lead-based compounds excess lead is typically added to the precursors to compensate for the evaporation of lead at high temperature,<sup>38–40</sup> motivates the need for a systematic study of the impact of cation nonstoichiometry on the properties of  $PbZrO_3$ .

In this spirit, we explore the effects of cation stoichiometry on antiferroelectric–ferroelectric phase stability, structural distortions, and field-dependent polarization behavior of  $Pb_{1+\delta}ZrO_3$  thin films. In this work, 50 nm thick  $Pb_{1+\delta}ZrO_3$  ( $\delta = 0, 0.1, 0.2$ ) thin films were synthesized via pulsed-laser deposition on 10 nm thick  $SrRuO_3$ -buffered  $DyScO_3$   $(110)$  substrates using lead-excess, lead zirconate ceramic targets of the same compositions. Single-phase  $Pb_{1+\delta}ZrO_3$  thin films with negligible differences in lattice parameters are revealed by X-ray diffraction despite Rutherford backscattering spectrometry (RBS) studies revealing large cation nonstoichiometry and heterostructures with nominal chemistries of  $PbZrO_3$ ,

$Pb_{1.1}ZrO_3$ , and  $Pb_{1.2}ZrO_3$ . Electrical characterization reveals that  $PbZrO_3$  and  $Pb_{1.1}ZrO_3$  heterostructures remain antiferroelectric, display double-hysteresis loops, and exhibit dielectric anomalies at  $\sim 290^\circ\text{C}$ , while  $Pb_{1.2}ZrO_3$  heterostructures exhibit single-hysteresis loops, indicative of ferroelectric response, with a broader dielectric response peaked at  $\sim 260^\circ\text{C}$ . Synchrotron-based X-ray reciprocal space mapping (RSM) studies further confirm the change in ordering with film chemistry wherein strong  $\frac{2\pi}{a}\left(\frac{1}{4}, 0, \frac{1}{4}\right)$  quarter-order diffraction peaks, indicative of antiferroelectric order, are observed in  $PbZrO_3$  and  $Pb_{1.1}ZrO_3$  heterostructures but not in  $Pb_{1.2}ZrO_3$  heterostructures. Density functional theory (DFT) calculations suggest that antisite  $Pb_{Zr}$  defects are the favorable point defects in lead-excess  $PbZrO_3$ , that such defects have a smaller formation energy in the metastable  $R3c$  ferroelectric phase than in the antiferroelectric  $Pbam$  phase, and that, in turn, the addition of the antisite defects can drive the system from the antiferroelectric  $Pbam$  phase toward the ferroelectric  $R3c$  phase.

## EXPERIMENTAL SECTION

**Thin-Film Synthesis and Chemical Analysis.** Fifty nanometer thick  $Pb_{1+\delta}ZrO_3$  thin films were grown on 10 nm  $SrRuO_3$ -buffered  $DyScO_3$   $(110)$  substrates (CrysTec GmbH) via reflection high-energy diffraction (RHEED)-assisted pulsed-laser deposition (Supporting Information, Figure S1) from ceramic targets of nominal stoichiometries of  $PbZrO_3$ ,  $Pb_{1.1}ZrO_3$ , and  $Pb_{1.2}ZrO_3$ . The  $SrRuO_3$  was grown at a heater temperature of  $680^\circ\text{C}$  in a dynamic oxygen pressure of 100 mTorr and with a laser fluence and repetition rate of  $1.0\text{ J/cm}^2$  and 5 Hz, respectively. For the various  $Pb_{1+\delta}ZrO_3$  films, growth was completed at a heater temperature of  $630^\circ\text{C}$  in a dynamic oxygen pressure of 80 mTorr and with a laser fluence and repetition rate of 1.8

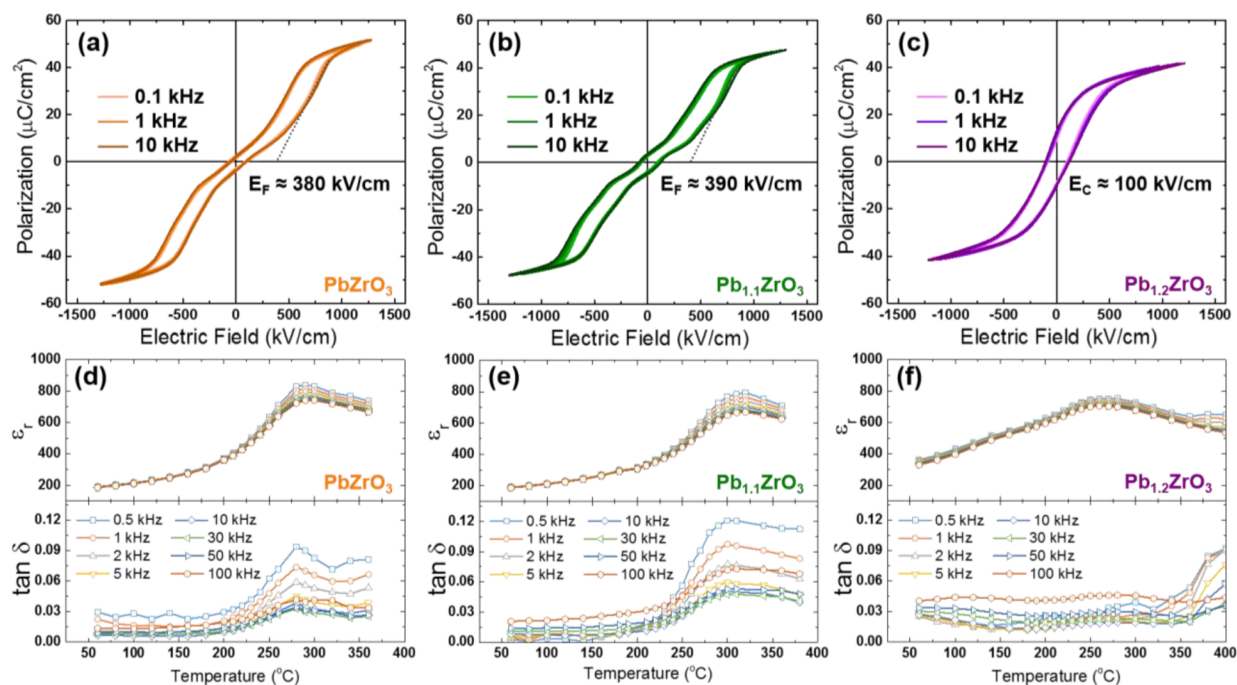


**Figure 2.** Ferroelectric polarization vs electric field hysteresis loops revealing antiferroelectric double-hysteresis loops for the (a) PbZrO<sub>3</sub> and (b) Pb<sub>1.1</sub>ZrO<sub>3</sub> heterostructures and ferroelectric-like single-hysteresis loops for (c) Pb<sub>1.2</sub>ZrO<sub>3</sub> heterostructures. Temperature-dependent dielectric permittivity (top) and loss tangent (bottom) probed as a function of frequencies reveal sharp dielectric anomalies for antiferroelectric (d) PbZrO<sub>3</sub> and (e) Pb<sub>1.1</sub>ZrO<sub>3</sub> heterostructures and a broader phase transition with no frequency-dispersion change across the transition temperature for the ferroelectric-like (f) Pb<sub>1.2</sub>ZrO<sub>3</sub> heterostructures.

J/cm<sup>2</sup> and 5 Hz, respectively. All films were grown in an on-axis geometry with a target-to-substrate distance of 5.2 cm. Following growth, the films were cooled to room temperature at a rate of 10 °C/min. in a static oxygen pressure of 700 Torr. The film chemistry was probed ex situ using RBS (incident ion energy 3040 keV, incident angle  $\alpha = 22.5^\circ$ , exit angle  $\beta = 25.35^\circ$ , and scattering angle  $\theta = 168^\circ$ ), and the spectra were fitted using the RBS analysis software SIMNRA.

**X-ray Diffraction Studies.** A high-resolution X-ray diffractometer (Panalytical, X'Pert<sup>3</sup> MRD) was used to perform line scans and preliminary RSM studies. Synchrotron X-ray RSM studies were conducted at the Advanced Photon Source, Argonne National Laboratory, Sector 33-BM using the Pilatus 100 K detector.

**Electrical Characterization.** Symmetric capacitor structures were fabricated by ex situ deposition of 100 nm thick, 25 μm diameter, circular SrRuO<sub>3</sub> top electrodes defined using an MgO hard-mask process.<sup>41</sup> Deposition of top electrodes was done at 500 °C and in a dynamic oxygen pressure of 100 mTorr to avoid significant lead loss. Other than temperature, the same growth conditions were used for the top SrRuO<sub>3</sub> growth as for the bottom electrodes. Ferroelectric polarization hysteresis loops were measured using a Precision Multiferroic Tester (Radiant Technologies), and dielectric and loss tangent measurements were performed using an E4890 LCR meter (Agilent/Keysight).

**First-Principles Calculations.** DFT calculations are performed within a revised generalized gradient approximation of Perdew–Burke–Ernzerhof (PBEsol)<sup>42</sup> with VASP.<sup>43</sup> The calculations use a plane-wave basis and an energy cutoff of 500 eV, gamma-centered *k*-point grid, and projected augmented wave pseudopotentials with 14, 12, and 6 valence electrons for Pb, Zr, and O, respectively, from the VASP library.<sup>44</sup> Structural relaxations are performed until atomic forces are <0.01 eV/Å. Antisite defects are simulated in supercells containing 32 formula units with 5 atoms/formula unit. We consider Pb:Zr ratios of 33:31, 34:30, and 35:29, corresponding to Pb<sub>1+δ</sub>ZrO<sub>3</sub> with δ = 0.06, 0.13, and 0.21, respectively. The formation energy of a Pb<sub>Zr</sub> antisite is computed by replacing a zirconium atom with a lead atom and fully relaxing the atomic coordinates and lattice constants. The formation energy of stoichiometric PbZrO<sub>3</sub> is given by  $H_F = E_{PZO}$

–  $E_{PbO} - E_{ZrO_2}$ , where  $E_{PZO}$ ,  $E_{PbO}$ , and  $E_{ZrO_2}$  correspond to the total energies of PbZrO<sub>3</sub>, PbO, and ZrO<sub>2</sub>, respectively.<sup>35</sup> The antisite formation energy is given by  $E_{Pb_{Zr}} = E_{Def} - E_{PZO} - E_{PbO_2} + E_{ZrO_2}$ , where  $E_{Def}$  is the total energy of a supercell containing one Pb<sub>Zr</sub>-antisite defect, and corresponds to the total energy of PbO<sub>2</sub>.<sup>35</sup> In addition, the formation energies of Pb, Zr, and O vacancies at relevant charge states, as well as lead and zirconium antisites, as a function of Fermi energy are computed. Charged defects are simulated by adding or removing electrons in the supercell and by adding a compensating uniform background charge. In this case, we assume oxygen-rich growth conditions and the corresponding chemical potentials.<sup>34</sup> Polarization calculations are performed from Berry phases using the modern theory of polarization,<sup>45</sup> as implemented in VASP. Further details of the calculations are in the [Supporting Information](#).

## RESULTS AND DISCUSSION

In stoichiometric PbZrO<sub>3</sub>, the room temperature *Pbam* ground state structure is related to the high-temperature cubic *Pm3m* perovskite structure by the combined distortion of two lattice modes: the antipolar displacement of the lead atoms ( $\Sigma$  mode) and the antiferrodistortive oxygen octahedral rotations (*R* mode). These collective distortions lower the symmetry of the cubic lattice and lead to an orthorhombic unit cell with lattice parameters  $a = 5.882 \text{ \AA}$ ,  $b = 8.228 \text{ \AA}$ , and  $c = 11.783 \text{ \AA}$ .<sup>11,12,46,47</sup> X-ray line-scans indicate that the films are (120)<sub>O</sub>-oriented (i.e., the film [120]<sub>O</sub> is parallel to the substrate normal [110]<sub>O</sub> where “O” denotes orthorhombic indices) for all three target chemistries (Figure 1a).<sup>48,49</sup> Further examination of the X-ray line scans ([Supporting Information](#), Figure S2) and RSMs (Figures 1b–d) for all three heterostructure variants reveals that all Pb<sub>1+δ</sub>ZrO<sub>3</sub> films are single phase and exhibit essentially identical lattice parameters regardless of the target chemistry. Note that the coexistence of 90° structural domains in PbZrO<sub>3</sub>, which has been observed previously,<sup>50,51</sup> should correspond to

440<sub>O</sub>- and 280<sub>O</sub>-diffraction peaks in the RSM scans. Despite no clear separation between these peaks in the laboratory-based RSM studies, later synchrotron-based studies show both are present but likely unresolvable due to the small lattice distortion in PbZrO<sub>3</sub>.<sup>46,47</sup> Additionally, the three heterostructure variants have essentially equal crystalline quality as indicated by the presence of strong Laue fringes and nearly identical rocking-curve full-width-at-half-maximum (fwhm  $\approx$  0.025°) values (Supporting Information, Figures S2b–d). Initial analysis of the structural data suggests that all three heterostructure variants, despite being grown from different target compositions, have the same structure. Studies of the film chemistry using RBS (Figures 1e–g) reveal that the resulting films are in fact stoichiometric replications of the targets with nominal chemistries of PbZrO<sub>3</sub>, Pb<sub>1.1</sub>ZrO<sub>3</sub>, and Pb<sub>1.2</sub>ZrO<sub>3</sub>. The latter implies that at least 20% lead excess can be accommodated in the lattice without a significant change in the lattice or deterioration of the film crystallinity. Such a finding is, at face value, intriguing and suggests a need for careful analysis of PbZrO<sub>3</sub> materials produced from lead-rich starting chemistries since basic structural characterization may not directly reflect these variations.

In turn, before exploring a more thorough analysis of the defect structures of these films, we first examine how the cation nonstoichiometry in Pb<sub>1+ $\delta$</sub> ZrO<sub>3</sub> affects the electrical properties. Polarization–electric field hysteresis loops and dielectric permittivity as a function of frequency and temperature were measured for the three different Pb<sub>1+ $\delta$</sub> ZrO<sub>3</sub> heterostructure variants (Figure 2). For the PbZrO<sub>3</sub> (Figure 2a) and Pb<sub>1.1</sub>ZrO<sub>3</sub> (Figure 2b) heterostructures, double-hysteresis loops (here shown for frequencies from 0.1 to 10 kHz), typical for an antiferroelectric, are observed for both stoichiometries with a saturated polarization of  $\sim$ 50  $\mu$ C/cm<sup>2</sup> and similar switching forward field values (380 and 390 kV/cm, respectively). Studies of the Pb<sub>1.2</sub>ZrO<sub>3</sub> heterostructures (Figure 2c), however, reveal the presence of a single-hysteresis loop indicative of ferroelectric-like response. The coercive field for the ferroelectric-like Pb<sub>1.2</sub>ZrO<sub>3</sub> heterostructures is  $\sim$ 100 kV/cm, and the saturation polarization is  $\sim$ 40  $\mu$ C/cm<sup>2</sup>, slightly smaller than the antiferroelectric samples. Different from antiferroelectric PbZrO<sub>3</sub> where the remnant polarization is close to zero at zero field, the Pb<sub>1.2</sub>ZrO<sub>3</sub> heterostructures exhibit a remnant polarization of  $\sim$ 10  $\mu$ C/cm<sup>2</sup>. Further study of the dielectric permittivity as a function of temperature reveals that both the antiferroelectric PbZrO<sub>3</sub> and Pb<sub>1.1</sub>ZrO<sub>3</sub> heterostructures (Figures 2d,e) exhibit a relatively sharp anomaly at  $\sim$ 290 °C and that the loss tangent remains low for frequencies ranging from 0.5 to 100 kHz. Similar studies of the ferroelectric-like Pb<sub>1.2</sub>ZrO<sub>3</sub> heterostructures (Figure 2f) reveal considerably broadened temperature dependence of the permittivity (which gradually peaks around  $\sim$ 260 °C) and essentially flat loss tangent at all temperatures measured (except at the highest temperatures, likely due to increased conduction of the sample). Furthermore, no obvious changes in the frequency dispersion of the dielectric permittivity or permittivity peak shifts as a function of frequency were observed for all heterostructures across the temperature range studied.

From these measurements, we can conclude that cation nonstoichiometry can dramatically change the electrical properties of Pb<sub>1+ $\delta$</sub> ZrO<sub>3</sub> such that antiferroelectricity is no longer manifested in the Pb<sub>1.2</sub>ZrO<sub>3</sub> heterostructures. We further propose that the electrical behavior of the Pb<sub>1.2</sub>ZrO<sub>3</sub> heterostructures is indicative of true ferroelectricity, not

spurious effects arising from leakage or otherwise. This is consistent with current–voltage studies (Supporting Information, Figure S3a) as well as the low loss tangent (as a function of frequency; Supporting Information, Figure S3b) at room temperature for all three heterostructure variants which shows that the samples are quite insulating and should have minimal leakage-related contributions to the ferroelectric hysteresis loops. Also, the ferroelectric nature of the Pb<sub>1.2</sub>ZrO<sub>3</sub> heterostructures is further supported by frequency-dependent hysteresis loops at room temperature (a wider range of frequencies, from 0.0001 to 100 kHz, is provided; Supporting Information, Figure S3c) which show that the coercive field increases systematically with frequency and that polarization saturates to the same level, with the same profile, indicating that the effects likely arise from switched polarization.<sup>52</sup> Current hysteresis loops also exhibit a single switching peak at low fields and remain essentially constant above the saturation field, again indicating the ferroelectric nature of the Pb<sub>1.2</sub>ZrO<sub>3</sub> heterostructures (Supporting Information, Figure S3d). Furthermore, the nature of the temperature- and frequency-dependent dielectric response of the Pb<sub>1.2</sub>ZrO<sub>3</sub> heterostructures suggests a homogeneous bulk response, instead of inhomogeneously polarized nanoregions where strong frequency-dependent dispersion in dielectric permittivity would be expected in the low-temperature regime.<sup>53,54</sup> Taken together, the data suggest that the Pb<sub>1.2</sub>ZrO<sub>3</sub> heterostructures are intrinsically ferroelectric, which implies that the structure of the film must be different from the antiferroelectric PbZrO<sub>3</sub> and Pb<sub>1.1</sub>ZrO<sub>3</sub> heterostructures.

To confirm this point, synchrotron-based X-ray RSM studies were performed. In antiferroelectric PbZrO<sub>3</sub>, the frozen  $\Sigma$  mode that gives rise to the antiparallel displacement of the lead atoms also gives rise to  $\frac{2\pi}{a}(\frac{1}{4}, 0, \frac{1}{4})$  quarter-order diffraction peaks, in a pseudocubic unit cell where  $a$  is the pseudocubic unit cell lattice constant.<sup>46,47,55</sup> Such diffraction peaks would not be observed in a ferroelectric phase. In turn, RSM studies about the DyScO<sub>3</sub> 332<sub>O</sub>-diffraction condition were undertaken (Figures 3a–c). These RSM studies reveal a number of interesting points. First, the scans show evidence of a predominantly relaxed film, but with a small fraction of coherently strained material. Both the relaxed and strained peaks (labeled as “R” and “S”, respectively) can be observed for all heterostructures. This finding is consistent with the growth mode observed by RHEED (Supporting Information, Figure S1). Briefly, the RHEED analysis reveals a Stranski–Krastanov-like growth mode wherein the film relaxes and transitions from 2D to 3D growth after 2–3 unit cells as evidenced by 2–3 oscillations of the RHEED intensity followed by an intensity drop and corresponding transition from streaks to dots in the diffraction pattern. The strained layer observed by the synchrotron-based X-ray RSM likely corresponds to those initial 2–3 unit cells. Second, the scans show marked variations in the intensity of the quarter-order diffraction peaks. The main Pb<sub>1+ $\delta$</sub> ZrO<sub>3</sub> diffraction conditions are indexed as 440<sub>O</sub> and 280<sub>O</sub>, while the quarter-order Bragg diffraction conditions from the antiparallel displaced lead atoms are indexed as 450<sub>O</sub> and 290<sub>O</sub>. Examination of the RSMs for the PbZrO<sub>3</sub> and Pb<sub>1.1</sub>ZrO<sub>3</sub> heterostructures reveals the presence of both the main and quarter-order diffraction peaks, clearly revealing antiferroelectric order and the coexistence of 90° antiferroelectric domains (Figures 3a,b). Similar examination of the RSMs for the Pb<sub>1.2</sub>ZrO<sub>3</sub> heterostructures, however, reveals considerably

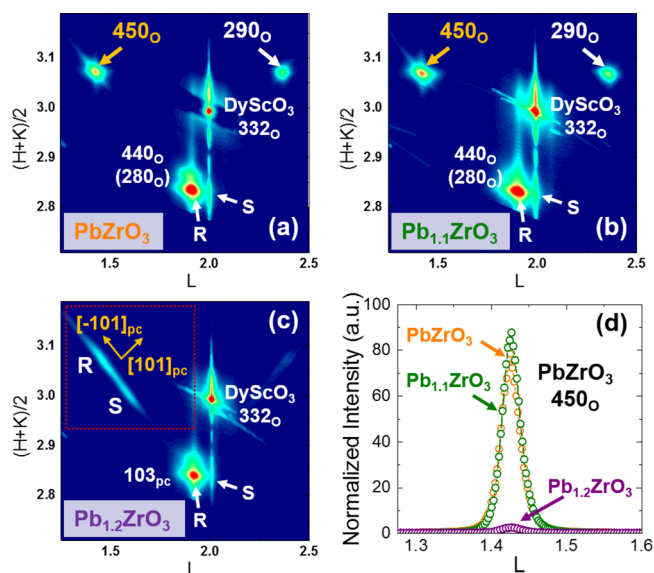


**Figure 3.** Synchrotron-based X-ray reciprocal space mapping studies about the around  $332_{\text{O}}$ -diffraction condition of the  $\text{DyScO}_3$  substrate for the (a)  $\text{PbZrO}_3$ , (b)  $\text{Pb}_{1.1}\text{ZrO}_3$ , and (c)  $\text{Pb}_{1.2}\text{ZrO}_3$  heterostructures. Data is plotted in reciprocal  $HKL$  vector space with respect to the  $\text{DyScO}_3$  orthorhombic lattice such that  $[0\ 0\ L]$  is the in-plane axis and  $[H\ K\ 0]$  is the out-of-plane axis. Relaxed and strained peaks from the  $\text{Pb}_{1+\delta}\text{ZrO}_3$  are labeled as “R” and “S”, respectively. Quarter-order Bragg peaks ( $450_{\text{O}}$  and  $290_{\text{O}}$ ) are observed for the  $\text{PbZrO}_3$  and  $\text{Pb}_{1.1}\text{ZrO}_3$  heterostructures, while diffused patterns along the  $[\bar{1}01]_{\text{pc}}$  are observed for the  $\text{Pb}_{1.2}\text{ZrO}_3$  heterostructures. (d)  $450_{\text{O}}$ -diffraction peak intensity normalized with respect to the substrate along the  $L$ -direction reveals strong Bragg diffraction for antiferroelectric  $\text{PbZrO}_3$  and  $\text{Pb}_{1.1}\text{ZrO}_3$  heterostructures but 2 orders of magnitude lower intensity in the ferroelectric-like  $\text{Pb}_{1.2}\text{ZrO}_3$  heterostructures.

reduced intensity of the quarter-order Bragg peaks (Figure 3c). Plotting the dominant  $450_{\text{O}}$ -diffraction condition intensity, normalized with respect to the substrate intensities, further reveals that for both the  $\text{PbZrO}_3$  and  $\text{Pb}_{1.1}\text{ZrO}_3$  heterostructures a sharp Bragg peak can be observed and that the  $\text{Pb}_{1.2}\text{ZrO}_3$  heterostructures exhibit a peak 2 orders of magnitude lower in diffraction intensity (Figure 3d). We note that the  $450_{\text{O}}$ -diffraction condition from the  $\text{Pb}_{1.2}\text{ZrO}_3$  heterostructures does not disappear completely but becomes diffusive and elongated along the  $[\bar{1}01]_{\text{pc}}$  (dashed square, Figure 3c). The narrow and elongated peak profile suggests a limited fraction of a strongly anisotropic antiferroelectrically ordered phase is

present.<sup>56</sup> Using standard Lorentzian fits of the diffuse scattering intensity,<sup>57</sup> the correlation length of the antiferroelectric ordering along the  $[\bar{1}01]_{\text{pc}}$  and  $[101]_{\text{pc}}$  can be approximated to be  $\lambda_{[\bar{1}01]_{\text{pc}}} \approx 3_{\text{nm}}$  and  $\lambda_{[101]_{\text{pc}}} > 30_{\text{nm}}$  (Supporting Information, Figure S4). Note also that there is weak, diffuse intensity about the  $290_{\text{O}}$ -diffraction condition, suggesting four variants of this scattering may be present. This means that the small fraction of antiferroelectrically-ordered phase would be shaped as thin “discs” or “sheet” with the normal of the flat surface pointing along the  $[\bar{1}01]_{\text{pc}}$ . To summarize, both the electrical and structural characterization point to the fact that excess-lead content in  $\text{PbZrO}_3$  drives the material away from the antiferroelectric ground state toward a ferroelectric state. The presence of what appears to be a residual antiferroelectric minority phase in the  $\text{Pb}_{1.2}\text{ZrO}_3$  heterostructures further suggests that this transition is gradual in nature and is consistent with the nearly energy-degenerate nature of the two possible phases in  $\text{PbZrO}_3$ .

To better understand this evolution and competition, we turned to first-principles calculations to explore the nature of the defects and the effects of cation nonstoichiometry on the energy competition between the antiferroelectric and ferroelectric phases. Based on the observed lead excess from RBS and the high-quality nature of the films observed via X-ray diffraction, we expect that the primary defect type corresponds to point defects which leads to a few possibilities: zirconium vacancies ( $V_{\text{Zr}}^{\text{IV}}$ ) or lead-antisite defects ( $\text{Pb}_{\text{Zr}}^{\text{II}}$  or  $\text{Pb}_{\text{Zr}}^{\text{IV}}$ ). Because the lattice does not show dramatic expansion with the increasing lead nonstoichiometry, one might expect that there is not a large concentration of either the ( $V_{\text{Zr}}^{\text{IV}}$ ) or  $\text{Pb}_{\text{Zr}}^{\text{IV}}$  defects, both of which would drive a change in the lattice parameters of the material and potentially a corresponding large concentration of compensating anion defects. These initial observations are supported by the results of the DFT calculations, which show good agreement (<1% difference) between the computed and experimental lattice constants for pristine  $\text{PbZrO}_3$  (Supporting Information, Table S1) and a negligible increase of the lattice parameters of 0.1%, 0.3%, and 0.5% for one, two, and three lead-antisite substitution. In addition, calculations of the formation energy of the various defects show that lead-antisite defects have a much smaller formation energy than that for the zirconium vacancies (Figure 4a; Supporting Information, Figure S5). In fact, the formation energy calculations suggest that creating  $\text{PbZrO}_3$  with even a small amount of lead excess—accommodated by lead antisites—is

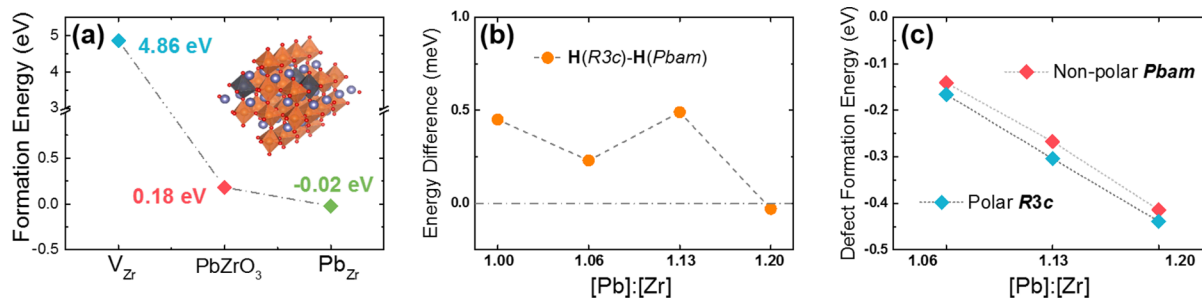


**Figure 4.** (a) Formation energies at  $T = 0\ \text{K}$  of stoichiometric  $\text{PbZrO}_3$ , zirconium vacancies ( $V_{\text{Zr}}$ ), and antisite defects ( $\text{Pb}_{\text{Zr}}$ ) in the  $\text{Pbam}$   $\text{PbZrO}_3$  lattice. Stoichiometric  $\text{PbZrO}_3$  is suggested to be metastable at low temperature while antisite defect formation in  $\text{PbZrO}_3$  lattice is unavoidable. (b) The energy difference between  $\text{R3c}$  and  $\text{Pbam}$  phases in nonstoichiometric  $\text{Pb}_{1+\delta}\text{ZrO}_3$  is small and remains <1 meV across the range of chemistries probed herein. (c) Antisite defects ( $\text{Pb}_{\text{Zr}}$ ) can form in both  $\text{Pbam}$  and  $\text{R3c}$   $\text{Pb}_{1+\delta}\text{ZrO}_3$  films, while such defects are more favored in the  $\text{R3c}$  phase as suggested by the lower defect formation energy across the entire doping range.

more energetically favorable than creating stoichiometric  $\text{PbZrO}_3$ . These results are consistent with previously reported defect studies on  $\text{PbZrO}_3$ .<sup>34–37</sup> In addition, examination of the Born effective charge shows that the valence state of the lead ions increases from +3.2 to +4.8 when they are located at the lead antisite (Supporting Information, Table S2), which indicates that lead is in a higher valence state on the zirconium site; in this manner, the system achieves charge neutrality in the system without the need to introduce additional point defects or charge carriers, consistent with our experimental findings that all three lead-excess samples remain electrically insulating. Also, the transition to a higher valence state for the lead-antisite defect is accompanied by a decrease in ionic radius (the Shannon–Prewitt ionic radii for  $\text{Pb}^{2+}$ ,  $\text{Pb}^{4+}$ , and  $\text{Zr}^{4+}$  in sixfold coordination are 1.19, 0.775, and 0.72 Å)<sup>58</sup> such that very little lattice distortion is expected for the system including significant lead-antisite defects. Directly probing such a small concentration of point defects is, however, difficult. In the absence of direct probes, one qualitative approach utilizes X-ray absorption near edge spectroscopy (XANES) at lead *L*-edge. Such studies revealed that the local coordination environment for lead ions in  $\text{Pb}_{1.2}\text{ZrO}_3$  heterostructures has changed with respect to antiferroelectric  $\text{PbZrO}_3$  and  $\text{Pb}_{1.1}\text{ZrO}_3$  (Supporting Information, Figure S6). Again, the small concentration of lead antisites prohibits quantification of the changes, but it does further suggest that some fraction of the lead ions in the system is occupying *B*-sites as antisite defects.

With this understanding of the nature of defects in the system, we proceed to examine their effect on the relative stability of the antiferroelectric and ferroelectric phases. To do this, we consider the relative energy stability of several polar structures with respect to the orthorhombic *Pbam* ground state. The competing polar structures of  $\text{PbZrO}_3$  are obtained by freezing in the unstable zone-center polar mode along different crystallographic directions, in combination with different oxygen octahedral patterns. In agreement with previous results,<sup>10,23</sup> the first-principles calculations show that the lowest energy structures correspond to the orthorhombic *Pbam* and rhombohedral *R3c* structures (Supporting Information, Table S3). These results confirm the *Pbam* structure as the lowest-energy antiferroelectric phase and suggest that the nearly energetically degenerate *R3c* polar structure most likely corresponds to the field-induced ferroelectric phase observed here for  $\text{PbZrO}_3$ . We find a small volume difference between *Pbam* and *R3c* of +0.5%. The computed macroscopic polarization is found to be  $59 \mu\text{C}/\text{cm}^2$ , in good agreement with the saturated polarization for pristine  $\text{PbZrO}_3$ .

Focusing on the *Pbam* and *R3c* structures, we next explore the energy evolution as a function of the lead-antisite content by computing the energy difference between the *Pbam* and *R3c* structures with  $[\text{Pb}]:[\text{Zr}] = 1.00, 1.06, 1.13, \text{ and } 1.20$  cation ratios, assuming the appropriate fraction of lead-antisite defects (Figure 4b). Across this range of cation ratios, the calculations reveal that the energy difference between the *Pbam* and *R3c* structures remains small, approximately  $\sim 1$  meV per formula unit, with increasing lead content (purple data, right axis, Figure 4b). While the exact energy difference between the *Pbam* and *R3c* structures depends on the choice of functional, we expect similar qualitative results for other functionals. For comparison, the energy difference between the *Pbam* and *R3c* structures is found to be  $\sim 4$  meV per formula unit across the range of cation ratios using the local density approximation (LDA).<sup>59</sup> The latter suggests that the structures remain nearly energeti-

cally degenerate as the lead content increases and that the ferroelectric order arises due to the energetic cost of defect formation rather than a coherent structural phase transition. To understand this better, we calculated the defect formation energies across the same range of cation ratios for the *Pbam* and *R3c* structures. The calculations reveal that as the lead content is increased, the energy gain upon creation of such defects in the *R3c* structure is always larger than that for the *Pbam* structure (Figure 4c; Supporting Information, Table S4). Thus, we propose that since the energy difference between the *Pbam* and *R3c* structures remains small across the entire cation ratio range studied herein, incorporation of lead excess in the form of lead-antisite defects tips the energy balance in favor of the *R3c* structure as the cost of producing those defects is smaller in this structure, and this, in turn, gives rise to the ferroelectric order.

## CONCLUSION

To summarize, we have studied the effects of cation nonstoichiometry on the evolution of the structure, electrical and dielectric properties, and (anti)ferroelectric order in  $\text{Pb}_{1+\delta}\text{ZrO}_3$  thin films. High-quality  $\text{PbZrO}_3$ ,  $\text{Pb}_{1.1}\text{ZrO}_3$ , and  $\text{Pb}_{1.2}\text{ZrO}_3$  thin films showing negligible differences in the lattice parameters have been produced. Subsequent studies reveal that the  $\text{PbZrO}_3$  and  $\text{Pb}_{1.1}\text{ZrO}_3$  heterostructures exhibit the expected antiferroelectric behavior and structure along with a relatively sharp phase transition at  $\sim 290$  °C.  $\text{Pb}_{1.2}\text{ZrO}_3$  heterostructures, however, likely exhibit rhombohedral symmetry and ferroelectric response along with a broader phase transition that peaks at  $\sim 260$  °C. In turn, synchrotron-based RSMs of the  $\text{Pb}_{1.2}\text{ZrO}_3$  heterostructures reveal dramatically suppressed peak intensities for quarter-order Bragg peaks expected for the orthorhombic, antiferroelectric phase—confirming the likely rhombohedral and ferroelectric nature of the nonstoichiometric samples. DFT calculations suggest that excess lead in the system is incorporated in the form of lead antisites, that the cost to form those defects is lower in the rhombohedral phase, and that, since the energy difference between the orthorhombic (antiferroelectric) and rhombohedral (ferroelectric) structures remains small across the entire cation ratio range studied herein, incorporation of lead excess in the form of lead-antisite defects tips the energy balance in favor of the *R3c* structure and results in the ferroelectric order. These results reveal the important role of cation stoichiometry in governing the competition between phases in complex materials such as the  $\text{PbZrO}_3$  system and provides a potential pathway by which one can control the properties of such materials.

## ASSOCIATED CONTENT

### Supporting Information

The Supporting Information is available free of charge on the ACS Publications website at DOI: 10.1021/acs.chemmater.7b02506.

Details concerning the growth of the  $\text{Pb}_{1+\delta}\text{ZrO}_3$  thin films; additional structural and electrical characterization of those films; diffuse scattering pattern analysis; details of and additional data from density functional theory calculations; X-ray absorption near edge spectroscopy studies (PDF)

## AUTHOR INFORMATION

### Corresponding Author

\*E-mail: [lwmartin@berkeley.edu](mailto:lwmartin@berkeley.edu)

### ORCID

Zuhuang Chen: 0000-0003-1912-6490

Lane W. Martin: 0000-0003-1889-2513

### Author Contributions

The manuscript was written through contributions of all authors. All authors have given approval to the final version of the manuscript.

### Notes

The authors declare no competing financial interest.

## ACKNOWLEDGMENTS

R.G. acknowledges support from the National Science Foundation under grant OISE-1545907. S.E.R.-L. and J.B.N. acknowledge support from the Molecular Foundry (supported by the Office of Science, Office of Basic Energy Sciences, of the U.S. Department of Energy) and the Laboratory Directed Research and Development Program at the Lawrence Berkeley National Laboratory under contract no. DE-AC02-05CH11231. R.X. acknowledges support from the National Science Foundation under grant DMR-1708615. A.D. acknowledges support from U.S. Department of Energy, Office of Science, Office of Basic Energy Science, under award number DE-SC0012375 for the development and synthesis of the PbZrO<sub>3</sub> thin films. L.R.D. acknowledges support from the Gordon and Betty Moore Foundation's EPiQS Initiative, under grant GBMF5307. J.K. acknowledges support from the National Science Foundation under grant DMR-1608938. S.S. acknowledges support from the National Science Foundation under grant DMR-1451219. L.W.M. acknowledges support from the Army Research Office under grant W911NF-14-1-0104. This research used resources of the Advanced Photon Source operated for the U.S. Department of Energy (DOE) Office of Science by Argonne National Laboratory under contract no. DE-AC02-06CH11357.

## REFERENCES

- (1) Burn, I.; Smyth, D. M. Energy Storage in Ceramic Dielectrics. *J. Mater. Sci.* **1972**, *7*, 339–343.
- (2) Mischenko, A. S.; Zhang, Q.; Scott, J. F.; Whatmore, R. W.; Mathur, N. D. Giant Electrocaloric Effect in Thin-Film PbZr<sub>0.95</sub>Ti<sub>0.05</sub>O<sub>3</sub>. *Science* **2006**, *311*, 1270–1271.
- (3) Parui, J.; Krupanidhi, S. B. Electrocaloric Effect in Antiferroelectric PbZrO<sub>3</sub> Thin Films. *Phys. Status Solidi RRL* **2008**, *2*, 230–232.
- (4) Berlincourt, D. Transducers Using Forced Transitions Between Ferroelectric and Antiferroelectric States. *IEEE Trans. Sonics Ultrason.* **1966**, *13*, 116–124.
- (5) Uchino, K.; Nomura, S.; Cross, L. E.; Newnham, R. E.; Jang, S. J. Electrostrictive Effect in Perovskites and Its Transducer Applications. *J. Mater. Sci.* **1981**, *16*, 569–578.
- (6) Liu, H.; Dkhil, B. A Brief Review on The Model Antiferroelectric PbZrO<sub>3</sub> Perovskite-like Material. *Zeit. Kristallog. Crystall. Mater.* **2011**, *226*, 163–170.
- (7) Shirane, G.; Sawaguchi, E.; Takagi, Y. Dielectric Properties of Lead Zirconate. *Phys. Rev.* **1951**, *84*, 476–481.
- (8) Ostapchuk, T.; Petzelt, J.; Zelezny, V.; Kamba, S.; Bovtun, V.; Porokhonsky, V.; Pashkin, A.; Kuzel, P.; Glinchuk, M. D.; Bykov, I. P.; Gorshunov, B.; Dressel, M. Polar Phonons and Central Mode in Antiferroelectric PbZrO<sub>3</sub> Ceramics. *J. Phys.: Condens. Matter* **2001**, *13*, 2677–2689.

(9) Rabe, K. M. Antiferroelectricity in Oxides: A Reexamination. In *Functional Metal Oxides*; Wiley-VCH Verlag GmbH & Co.: Weinheim, Germany, 2013; pp 221–244.

(10) Singh, D. J. Structure and Energetics of Antiferroelectric PbZrO<sub>3</sub>. *Phys. Rev. B: Condens. Matter Mater. Phys.* **1995**, *52*, 12559–12563.

(11) Tagantsev, A. K.; Vaideswaran, K.; Vakhrushev, S. B.; Filimonov, A. V.; Burkovsky, R. G.; Shaganov, A.; Andronikova, D.; Rudskoy, A. I.; Baron, A. Q. R.; Uchiyama, H.; Chernyshov, D.; Bosak, A.; Ujma, Z.; Roleder, K.; Majchrowski, A.; Ko, J. H.; Setter, N. The Origin of Antiferroelectricity in PbZrO<sub>3</sub>. *Nat. Commun.* **2013**, *4*, 2229.

(12) Waghmare, U. V.; Rabe, K. M. Lattice Instabilities, Anharmonicity and Phase Transitions in PbZrO<sub>3</sub> from First Principles. *Ferroelectrics* **1997**, *194*, 135–147.

(13) Hao, X.; Zhai, J.; Yao, X. Improved Energy Storage Performance and Fatigue Endurance of Sr-Doped PbZrO<sub>3</sub> Antiferroelectric Thin Films. *J. Am. Ceram. Soc.* **2009**, *92*, 1133–1135.

(14) Shirane, G. Ferroelectricity and Antiferroelectricity in Ceramic PbZrO<sub>3</sub> Containing Ba or Sr. *Phys. Rev.* **1952**, *86*, 219–227.

(15) Cockayne, E.; Rabe, K. M. Pressure Dependence of Instabilities in Perovskite PbZrO<sub>3</sub>. *J. Phys. Chem. Solids* **2000**, *61*, 305–308.

(16) Mani, B. K.; Lisenkov, S.; Ponomareva, I. Finite-Temperature Properties of Antiferroelectric PbZrO<sub>3</sub> from Atomistic Simulations. *Phys. Rev. B: Condens. Matter Mater. Phys.* **2015**, *91*, 134112.

(17) Hung, C.-L.; Chueh, Y.-L.; Wu, T.-B.; Chou, L.-J. Characteristics of Constrained Ferroelectricity in PbZrO<sub>3</sub>/BaZrO<sub>3</sub> Superlattice Films. *J. Appl. Phys.* **2005**, *97*, 034105.

(18) Kanno, I.; Hayashi, S.; Takayama, R.; Hirao, T. Superlattices of PbZrO<sub>3</sub> and PbTiO<sub>3</sub> Prepared by Multi-Ion-Beam Sputtering. *Appl. Phys. Lett.* **1996**, *68*, 328–330.

(19) Mani, B. K.; Chang, C. M.; Lisenkov, S.; Ponomareva, I. Critical Thickness for Antiferroelectricity in PbZrO<sub>3</sub>. *Phys. Rev. Lett.* **2015**, *115*, 097601.

(20) Woodward, D. I.; Knudsen, J.; Reaney, I. M. Review of Crystal and Domain Structures in the PbZr<sub>x</sub>Ti<sub>1-x</sub>O<sub>3</sub> Solid Solution. *Phys. Rev. B: Condens. Matter Mater. Phys.* **2005**, *72*, 104110.

(21) Ge, J.; Remiens, D.; Dong, X.; Chen, Y.; Costecalde, J.; Gao, F.; Cao, F.; Wang, G. Enhancement of Energy Storage in Epitaxial PbZrO<sub>3</sub> Antiferroelectric Films Using Strain Engineering. *Appl. Phys. Lett.* **2014**, *105*, 112908.

(22) Pisarski, M.; Ujma, Z.; Hańderek, J. The Influence of Hydrostatic Pressure on Phase Transitions in PbZrO<sub>3</sub> with Pb and O Vacancies. *Phase Transitions* **1984**, *4*, 157–167.

(23) Reyes-Lillo, S. E.; Rabe, K. M. Antiferroelectricity and Ferroelectricity in Epitaxially Strained PbZrO<sub>3</sub> from First Principles. *Phys. Rev. B: Condens. Matter Mater. Phys.* **2013**, *88*, 180102.

(24) Roy Chaudhuri, A.; Arredondo, M.; Hähnel, A.; Morelli, A.; Becker, M.; Alexe, M.; Vrejoiu, I. Epitaxial Strain Stabilization of A Ferroelectric Phase in PbZrO<sub>3</sub> Thin Films. *Phys. Rev. B: Condens. Matter Mater. Phys.* **2011**, *84*, 054112.

(25) Boldyreva, K.; Pintilie, L.; Lotnyk, A.; Misirlioglu, I. B.; Alexe, M.; Hesse, D. Thickness-Driven Antiferroelectric-to-Ferroelectric Phase Transition of Thin PbZrO<sub>3</sub> Layers in Epitaxial PbZrO<sub>3</sub>/Pb(Zr<sub>0.8</sub>Ti<sub>0.2</sub>)O<sub>3</sub> Multilayers. *Appl. Phys. Lett.* **2007**, *91* (12), 122915.

(26) Breckenfeld, E.; Wilson, R.; Karthik, J.; Damodaran, A. R.; Cahill, D. G.; Martin, L. W. Effect of Growth Induced (Non)-Stoichiometry on the Structure, Dielectric Response, and Thermal Conductivity of SrTiO<sub>3</sub> Thin Films. *Chem. Mater.* **2012**, *24*, 331–337.

(27) Brooks, C. M.; Wilson, R. B.; Schäfer, A.; Mundy, J. A.; Holtz, M. E.; Muller, D. A.; Schubert, J.; Cahill, D. G.; Schlom, D. G. Tuning Thermal Conductivity in Homoepitaxial SrTiO<sub>3</sub> Films via Defects. *Appl. Phys. Lett.* **2015**, *107*, 051902.

(28) Tenne, D. A.; Farrar, A. K.; Brooks, C. M.; Heeg, T.; Schubert, J.; Jang, H. W.; Bark, C. W.; Folkman, C. M.; Eom, C. B.; Schlom, D. G. Ferroelectricity in Nonstoichiometric SrTiO<sub>3</sub> Films Studied by Ultraviolet Raman Spectroscopy. *Appl. Phys. Lett.* **2010**, *97*, 142901.

(29) Lee, J.-K.; Hong, K.-S.; Jang, J.-W. Roles of Ba/Ti Ratios in the Dielectric Properties of BaTiO<sub>3</sub> Ceramics. *J. Am. Ceram. Soc.* **2001**, *84*, 2001–2006.

- (30) Lee, S.; Liu, Z.-K.; Kim, M.-H.; Randall, C. A. Influence of Nonstoichiometry on Ferroelectric Phase Transition in BaTiO<sub>3</sub>. *J. Appl. Phys.* **2007**, *101*, 054119.
- (31) Dedon, L. R.; Saremi, S.; Chen, Z.; Damodaran, A. R.; Apgar, B. A.; Gao, R.; Martin, L. W. Nonstoichiometry, Structure, and Properties of BiFeO<sub>3</sub> Films. *Chem. Mater.* **2016**, *28*, 5952–5961.
- (32) Jang, H. W.; Kumar, A.; Denev, S.; Biegalski, M. D.; Maksymovych, P.; Bark, C. W.; Nelson, C. T.; Folkman, C. M.; Baek, S. H.; Balke, N.; Brooks, C. M.; Tenne, D. A.; Schlom, D. G.; Chen, L. Q.; Pan, X. Q.; Kalinin, S. V.; Gopalan, V.; Eom, C. B. Ferroelectricity in Strain-Free SrTiO<sub>3</sub> Thin Films. *Phys. Rev. Lett.* **2010**, *104*, 197601.
- (33) Damodaran, A. R.; Breckenfeld, E.; Chen, Z.; Lee, S.; Martin, L. W. Enhancement of Ferroelectric Curie Temperature in BaTiO<sub>3</sub> Films via Strain-Induced Defect Dipole Alignment. *Adv. Mater.* **2014**, *26*, 6341–6347.
- (34) Chotsawat, M.; Sarasamak, K.; Thanomngam, P.; T-Thienprasert, J. First-principles Study of Antisite Defects in Orthorhombic PbZrO<sub>3</sub>. *Integr. Ferroelectr.* **2014**, *156*, 86–92.
- (35) Kagimura, R.; Singh, D. J. Ab Initio Study of Pb Antisite Defects in PbZrO<sub>3</sub> and Pb(Zr,Ti)O<sub>3</sub>. *Phys. Rev. B: Condens. Matter Mater. Phys.* **2008**, *78*, 174105.
- (36) Suchanek, G.; Deyneka, A.; Jastrabik, L.; Savinov, M.; Gerlach, G. Lead Excess in Pb(Zr,Ti)O<sub>3</sub> Thin Films Deposited by Reactive Sputtering at Low Temperatures. *Ferroelectrics* **2005**, *318*, 3–10.
- (37) Whatmore, R. W.; Huang, Z.; Todd, M. Sputtered Lead Scandium Tantalate Thin Films: Pb<sup>4+</sup> in B Sites in The Perovskite Structure. *J. Appl. Phys.* **1997**, *82*, 5686–5694.
- (38) Harjuoja, J.; Väyrynen, S.; Putkonen, M.; Niinistö, L.; Rauhala, E. Atomic Layer Deposition of PbZrO<sub>3</sub> Thin Films. *Appl. Surf. Sci.* **2007**, *253*, 5228–5232.
- (39) Yadav, A. K.; Nelson, C. T.; Hsu, S. L.; Hong, Z.; Clarkson, J. D.; Schlepüetz, C. M.; Damodaran, A. R.; Shafer, P.; Arenholz, E.; Dedon, L. R.; Chen, D.; Vishwanath, A.; Minor, A. M.; Chen, L. Q.; Scott, J. F.; Martin, L. W.; Ramesh, R. Observation of Polar Vortices in Oxide Superlattices. *Nature* **2016**, *530*, 198–201.
- (40) Zhang, W.; Sasaki, K.; Hata, T. Analysis of Sputter Process on a New ZrTi+PbO Target System and Its Application to Low-Temperature Deposition of Ferroelectric Pb(Zr, Ti)O<sub>3</sub> Films. *Jpn. J. Appl. Phys.* **1996**, *35*, 1868–1872.
- (41) Karthik, J.; Damodaran, A. R.; Martin, L. W. Epitaxial Ferroelectric Heterostructures Fabricated by Selective Area Epitaxy of SrRuO<sub>3</sub> Using an MgO Mask. *Adv. Mater.* **2012**, *24*, 1610–1615.
- (42) Perdew, J. P.; Ruzsinszky, A.; Csonka, G. I.; Vydrov, O. A.; Scuseria, G. E.; Constantin, L. A.; Zhou, X.; Burke, K. Restoring the Density-Gradient Expansion for Exchange in Solids and Surfaces. *Phys. Rev. Lett.* **2008**, *100*, 136406.
- (43) Kresse, G.; Furthmüller, J. Efficient Iterative Schemes for *ab initio* Total-energy Calculations Using a Plane-wave Basis Set. *Phys. Rev. B: Condens. Matter Mater. Phys.* **1996**, *54*, 11169–11186.
- (44) Kresse, G.; Joubert, D. From Ultrasoft Pseudopotentials to the Projector Augmented-wave Method. *Phys. Rev. B: Condens. Matter Mater. Phys.* **1999**, *59*, 1758–1775.
- (45) King-Smith, R. D.; Vanderbilt, D. Theory of Polarization of Crystalline Solids. *Phys. Rev. B: Condens. Matter Mater. Phys.* **1993**, *47*, 1651–1654.
- (46) Fujishita, H.; Katano, S. Re-Examination of the Antiferroelectric Structure of PbZrO<sub>3</sub>. *J. Phys. Soc. Jpn.* **1997**, *66*, 3484–3488.
- (47) Fujishita, H.; Katano, S. Crystal Structure of Perovskite PbZrO<sub>3</sub> Re-investigated by High Resolution Powder Neutron Diffraction. *Ferroelectrics* **1998**, *217*, 17–20.
- (48) Boldyreva, K.; Bao, D.; Le Rhun, G.; Pintilie, L.; Alexe, M.; Hesse, D. Microstructure and Electrical Properties of (120)<sub>O</sub>-oriented and of (001)<sub>O</sub>-oriented Epitaxial Antiferroelectric PbZrO<sub>3</sub> Thin Films on (100) SrTiO<sub>3</sub> Substrates Covered with Different Oxide Bottom Electrodes. *J. Appl. Phys.* **2007**, *102*, 044111.
- (49) Pintilie, L.; Boldyreva, K.; Alexe, M.; Hesse, D. Coexistence of Ferroelectricity and Antiferroelectricity in Epitaxial PbZrO<sub>3</sub> Films with Different Orientations. *J. Appl. Phys.* **2008**, *103*, 024101.
- (50) Tanaka, M.; Saito, R.; Tsuzuki, K. Electron Microscopic Studies on Domain Structure of PbZrO<sub>3</sub>. *Jpn. J. Appl. Phys.* **1982**, *21*, 291–298.
- (51) Shen, G. J.; Lu, C. J.; Shen, H. M.; Wang, Y. N. Transmission Electron Microscopy Study of 180° Domain Structure in PbZrO<sub>3</sub>. *J. Mater. Sci. Lett.* **1997**, *16*, 880–882.
- (52) Scott, J. F. Ferroelectrics Go Bananas. *J. Phys.: Condens. Matter* **2008**, *20*, 021001.
- (53) Bokov, A. A.; Ye, Z. G. Recent Progress in Relaxor Ferroelectrics with Perovskite Structure. *J. Mater. Sci.* **2006**, *41*, 31–52.
- (54) Pokharel, B. P.; Ranjan, R.; Pandey, D.; Siruguri, V.; Paranjpe, S. K. Rhombohedral Superlattice Structure and Relaxor Ferroelectric Behavior of (Pb<sub>0.70</sub>Ba<sub>0.30</sub>)ZrO<sub>3</sub> Ceramics. *Appl. Phys. Lett.* **1999**, *74*, 756–758.
- (55) Shimizu, H.; Guo, H.; Reyes-Lillo, S. E.; Mizuno, Y.; Rabe, K. M.; Randall, C. A. Lead-free Antiferroelectric: xCaZrO<sub>3</sub>-(1-x)NaNbO<sub>3</sub> System (0 < x < 0.10). *Dalton Trans.* **2015**, *44*, 10763–10772.
- (56) Goossens, D. J. Diffuse Scattering from Lead-Containing Ferroelectric Perovskite Oxides. *ISRN Mater. Sci.* **2013**, *2013*, 1–17.
- (57) Xu, G.; Zhong, Z.; Hiraka, H.; Shirane, G. Three-Dimensional Mapping of Diffuse Scattering in Pb(Zn<sub>1/3</sub>Nb<sub>2/3</sub>)O<sub>3-x</sub>PbTiO<sub>3</sub>. *Phys. Rev. B: Condens. Matter Mater. Phys.* **2004**, *70*, 174109.
- (58) Shannon, R. Revised Effective Ionic Radii and Systematic Studies of Interatomic Distances in Halides and Chalcogenides. *Acta Crystallogr., Sect. A: Cryst. Phys., Diffr., Theor. Gen. Crystallogr.* **1976**, *32*, 751–767.
- (59) Perdew, J. P.; Zunger, A. Self-interaction Correction to Density-Functional Approximations for Many-electron Systems. *Phys. Rev. B: Condens. Matter Mater. Phys.* **1981**, *23*, 5048–5079.